OPEN

Correspondence and requests for materials should be addressed to M.A.H. (mohsenegypt@um. edu.my) or R.M. (mahmoodian.reza@ gmail.com)

Modified smoothed particle hydrodynamics (MSPH) for the analysis of centrifugally assisted TiC-Fe-Al$_2$O$_3$ combustion synthesis

M. A. Hassan[1,2], Reza Mahmoodian[1,3] & M. Hamdi[1]

[1]Centre of Advanced Manufacturing and Materials Processing (AMMP), Department of Mechanical Engineering, University of Malaya, 50603 Kuala Lumpur, Malaysia, [2]Department of Mechanical Engineering, Assiut University, Assiut 71516, Egypt, [3]Department of Research and Development, AzarinKar IND. Co., Industrial Zone 1, 7635168361 Kerman, Iran.

A modified smoothed particle hydrodynamic (MSPH) computational technique was utilized to simulate molten particle motion and infiltration speed on multi-scale analysis levels. The radial velocity and velocity gradient of molten alumina, iron infiltration in the TiC product and solidification rate, were predicted during centrifugal self-propagating high-temperature synthesis (SHS) simulation, which assisted the coating process by MSPH. The effects of particle size and temperature on infiltration and solidification of iron and alumina were mainly investigated. The obtained results were validated with experimental microstructure evidence. The simulation model successfully describes the magnitude of iron and alumina diffusion in a centrifugal thermite SHS and Ti + C hybrid reaction under centrifugal acceleration.

S elf-propagating high-temperature synthesis (SHS), or combustion synthesis (CS), is an advanced method of producing high-temperature materials, such as refractory or intermetallic materials and cermets. The CS process is characterized by extreme heating rates, short reaction times, and expelling impurities during reaction[1,2]. Ceramic-lined steel pipes are a sort of high-performance, heat-resistant, anti-corrosion and wear-resistant pipe that can be produced by a centrifugally-assisted thermite (CT) process[3]. The ceramic-lined steel pipe produced by SHS technique has occupied the market rapidly. Not only are the quality superior and the capabilities outstanding, but the price ratio is higher than of other wearable, anti-abrasion and anti-heat pipes. Moreover, they weigh less compared to other wearable, cast alloy steel pipes[4,5].

In a research by Gao, et al.[6], in China, W-C-Fe cermet-lined steel pipes were produced through a SHS-centrifugal process. Finite element analysis of residual thermal stress was performed on ceramic-lined composite pipes prepared by centrifugal SHS. The finite element method of simulating the temperature and residual thermal stress distribution of the ceramic-lined composite pipe made by centrifugal SHS was discussed. Wang and Yang[7] also employed various SHS layer thicknesses to fabricate centrifugal-SHS composite pipes with the aim of reducing residual stress. Therefore, the reliability of the ceramic-lined composite pipes should improve.

Local reinforcement of functionally graded coating produced using a centrifugal-assisted thermite process has recently come to the attention of researchers[8–10]. The thermite reaction (Al$_2$O$_3$ and Fe) infiltrated the TiC pellets and created a strong, titanium aluminide intermetallic layer. There is a compelling need to simulate the mechanism of locally reinforcing lined ceramic tubes. Several simulation techniques are applied in SHS, among which finite difference numerical method[11], numerical modeling of field-activated combustion synthesis process[12], modeling the solidification of functionally graded materials by centrifugal casting[10,13], and analytical modeling[14,15].

Initially developed in1977[16,17], Smoothed Particle Hydrodynamics (SPH) is a meshless Lagrangian particle method for obtaining approximate numerical solutions of fluid dynamics equations. The SPH method was originally meant for astrophysical applications. It gradually extended to problems concerning incompressible fluids using either weakly compressible fluid models, or algorithms designed to solve full incompressible equations[18]. In this method, the fluid is replaced by a set of particles[19,20]. At present, SPH has a wide range of applications in numerous fields, such as heat conduction, gas explosions, micromachining, micro-forming, and granular flows that have demonstrated the ability to simulate highly non-linear free-surface flows including
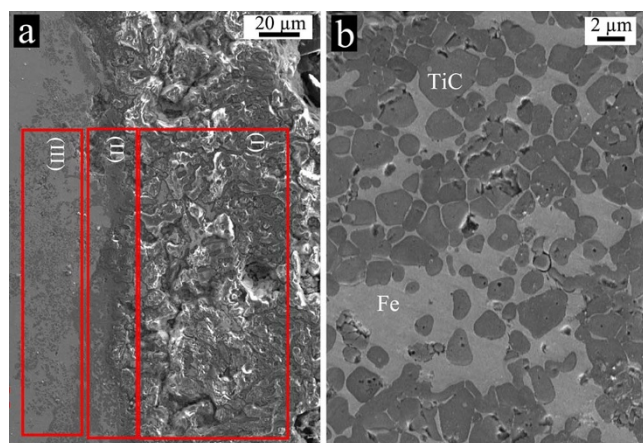
Figure 1 | FESEM microstructure of functionally graded TiC-Fe-Al2O3 coating; (a) Region next to the inner most layers relative to the pipe's axis: zone (I) Alumina-rich layer coating on the Ti + C pellet, (II) Ti-Fe-Al-rich zone intermetallic on the Ti + C pellet and the coated layer, (III) Fe-rich zone in the Ti + C pellet; (b) a higher magnification of zone (II).

wave overturning, jets, and the formation of spray and droplets[21,22]. SPH has been vastly developed for different applications like underwater explosion[20], wave propagation[19], magnetohydrodynamics[23], bulk deformation[24], and particle motion[18]. SPH has also been implemented to solve complex splashing free-surface flows and the differential motion of multiple solid-casting processes owing to its mesh-free nature. It can additionally handle boundaries and apply fragmenting free-surface flow of solid particles[25].

In the SPH technique, the spatial gradients of speed and deposition rate at the boundaries are difficult to calculate due to insufficient data. This method also employs ghost particles at the boundary, which are not real or adequate for solving approximation problems at the boundary. Therefore, to mitigate such drawbacks, modified smoothed particle hydrodynamics (MSPH) is adopted based on the Taylor expansion as opposed to ghost particles[26].

Mathematically, the range of problems that can be solved by MSPH is much broader than by mesh-based methods, since approximation is not based on elements whose distortion may degrade calculation accuracy, something helpful in both the fluid and solid domains[27]. However, to the best of the authors' knowledge, there are no reports on meshless particle methods such as MSPH to simulate SHS particle behavior, e.g., velocity, viscosity, and displacement.

Therefore, the purpose of this work is to implement MSPH to predict the radial velocity and velocity gradient of molten alumina, iron infiltration in the TiC product and solidification rate during the centrifugal SHS-assisted functional coating process. The effects of particle size and temperature on the infiltration and solidification of iron and alumina are mainly investigated. The obtained results are validated with experimental evidence of microstructure.

Results

Temperature data obtained from the solution of the heat balance equation was employed to calculate the fluids' (iron and alumina) viscosity, particle speed in the radial direction, gradient of speed, and particles' position. A microstructural analysis is also presented in this section. In order to verify the MSPH code, the exact solution of velocity equation (7) and values obtained from the MSPH solution are plotted accordingly. In addition, the measured temperatures are compared with the MSPH solution results from equation (6).

Microstructural analysis. A typical area of functionally graded TiC-Fe-Alumina functionally graded coating, processed using centrifugally assisted combustion synthesis method, was taken for microstructural observations. A field emission scanning electron

Table 1 | Elemental analysis of three zones relative to the pipe axis

Element	Zone (I)	Zone (II)	Zone (III)
C	3.69	5.83	9.32
O	35.77	28.23	3.9
Al	45.14	20.52	0.49
Ti	4.66	23.32	24.82
Fe	10.74	22.1	61.47

microscopy (FESEM) micrograph of the typical area is shown in Figure 1. Figure 1 (a) illustrates a region next to the pellet's inner surface relative to the rotation axis, while Figure 1 (b) depicts a higher magnification of zone (III) from Figure 1(a). Corresponding energy dispersive spectroscopy (EDS) elemental analysis of Figure 1 (a) for zones (I), (II), and (III) is listed in Table 1. Zones (I), (II), and (III) in Figure 1 (a) are marked relative to the tube's axis of rotation.

In accordance with the EDS and FESEM results, the thickness of the alumina-rich layer comprising zones (I) and (II) is roughly 110 μm. Moreover, zone (I) is a composite-coated layer with an alumina-rich constituent. However, based on micrograph measurements, alumina diffusion occurs around zone (II), whose thickness is around 30 μm. On the other hand, iron particles diffuse deeper into the Ti + C pellet compared with alumina.

Particle viscosity versus time. The time-viscosity plot of a centrifugal thermite reaction is illustrated in Figure 2 along with the corresponding temperature cooling reaction. The time-viscosity plot is the MSPH solution of the exact calculations using Arrhenius' equation adopted in eq. (8).

Particle velocity and velocity gradient. The exact particle solution is derived based on fundamentals of fluid mechanics, which provides a closed-form solution for the velocity and position of alumina and iron as given by equations (7) and (11). The exact solution of particle velocity and the corresponding MSPH simulation in three different particle size cases (dp, dp2, and dp3) are plotted in Figure 3. The simulation parameters are listed in Table 2.

Figure 4 shows the radial velocity of molten alumina particles for three different particle sizes as predicted by MSPH and the exact solution. Figure 5 illustrates the particle velocity gradient in the radial direction as estimated by equation (11) based on the MSPH model.

Change in particle position. The instantaneous change in radial particle position versus time during the deposition process is calculated for iron and alumina particles and the results are given in Figure 6. Evidently, there is an indirect correlation with viscosity change over time.

Discussion

Once the thermite reaction occurred under the influence of centrifugal acceleration, the molten Al_2O_3-Fe thermite products infiltrated the Ti + C pellet. The infrared pyrometer recorded the reaction temperature released up to 2830°C (Figure 2). The thermite molten products were pushed to the inner surface of the Ti + C pellet under the applied centrifugal force. The molten semi-products were forcibly trying to penetrate the porous Ti + C media to form an in-situ TiC-Fe-Al_2O_3 composite. According to the temperature observation, the reaction lasted around 2.5 seconds from ignition until Fe solidification, at which point the reaction and infiltration presumably stopped. The thermite reaction products (Fe and Al_2O_3) deposited according to their densities[28] at the graphite mold's innermost layer, after which they diffused into the TiC zone. The reactions created a porous TiC product. A more in-depth discussion on the current method is given elsewhere[8].

In Figure 1 (a), zone (I) is alumina-rich, and zones (II) and (III) are Fe-rich. Zone (I) is located at the innermost layer relative to the pipe's
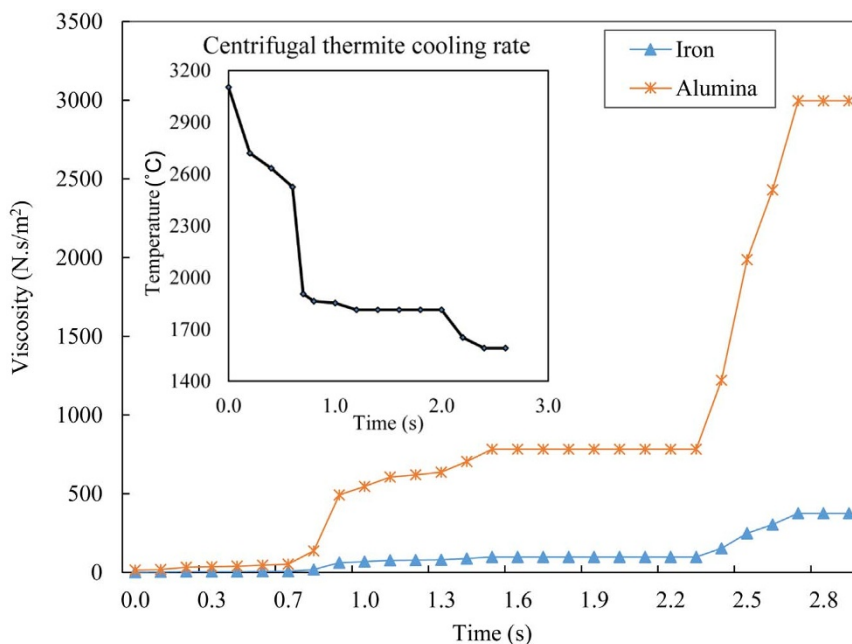
Figure 2 | Viscosity rate of iron and alumina products according to equation (6).

axis. Alumina mainly formed a coating layer on the TiC pellet and slightly diffused into it, whereas the iron phase mostly diffused inside the TiC pellet. The composition of the phases gradually changed with the specimen's volume. Figure 1 (b) represents the magnified micrograph corresponding to zone (III). It is clear how the molten iron diffused inside the porous area of the compacted Ti + C pellet and formed an interesting composite. Iron particles exist in all layers, with a declining rate from the inner to the outermost layer relative to the axis of rotation. Centrifugal acceleration significantly affected both metallurgical alloying and mechanical interlocking between different specimen layers during product formation. It is apparent

that the alumina phase did not significantly diffuse in zone (III), whereas the iron phase diffused into the TiC pellet.

As revealed in Figure 2, the viscosity of molten alumina particles exhibits higher values and abrupt changes at 0.8 and 2.4 s after the reaction started, compared to iron particles. This is because the melting point of alumina is above 2200°C and it starts to solidify at 0.7 s, while Fe is in a molten state seeing that its melting point is 1535°C. This explains why Fe was able to penetrate deeper into TiC, as well as according to the FESEM microstructure observation of Figure 1, zone (iii). The viscosity analysis serves to calculate the particle velocity and location at any given time.
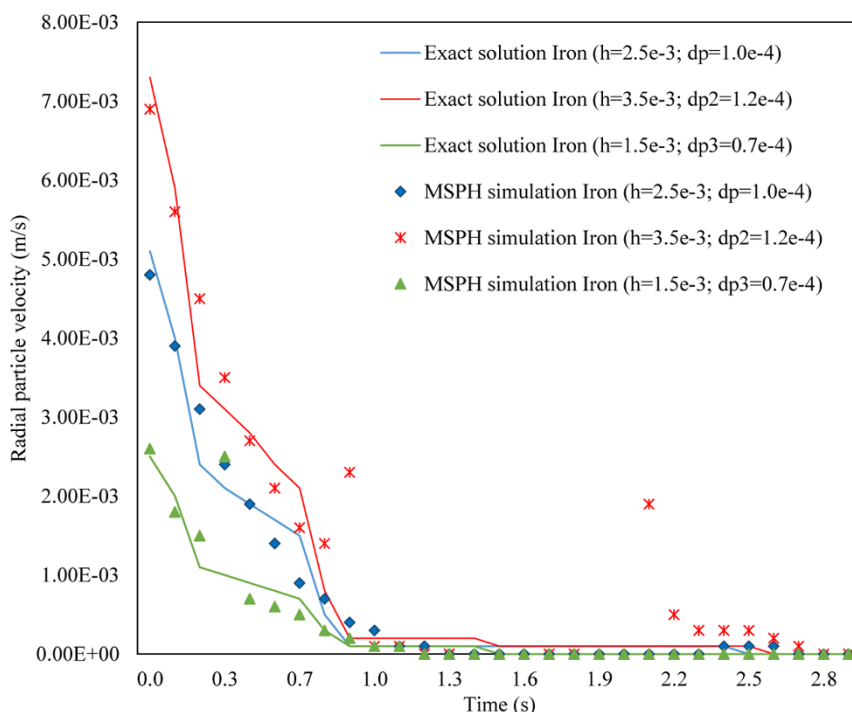

Figure 3 | Iron particle radial velocity versus time obtained from the analytical model and MSPH predictions for different particle sizes.

Table 2 | MSPH parameter of iron and alumina particles

Material	Particle Size code	Interaction radius: h (m)	Particle size dp(m)
Iron	dp	2.5×10^{-3}	1.0×10^{-4}
Iron	dp2	3.5×10^{-3}	1.2×10^{-4}
Iron	dp3	1.5×10^{-3}	0.7×10^{-4}
Alumina	dp	2.5×10^{-3}	1.0×10^{-4}
Alumina	dp2	3.5×10^{-3}	1.2×10^{-4}
Alumina	dp3	1.5×10^{-3}	0.7×10^{-4}

With respect to Figure 3, in the early process stages and shortly after the reaction began, the iron particles' radial velocity slowed down rapidly as viscosity increased. It completely stopped after three seconds of reaction process. Physically, the particle migration rate (particle velocity) becomes zero when the viscosity sharply increases during solidification or when the particles reach a boundary that halts further movement. Under the centrifugal field where the particles were larger, the initial speed would be higher, compared with the smaller particles. The particle velocity of MSPH prediction is in close correlation with the exact solution results from Figure 3. This validates the simulation model and permits for the application of MSPH in the SHS process. As seen in Figure 4, the alumina particle velocity seems to be approximately half the velocity of iron particles for corresponding particle sizes. This may be attributable to the density of iron, which is about twice that of alumina.

Equation (11) is simpler than deriving and using the exact expression for velocity gradient calculations. Obviously, the velocity gradient can describe continuous particle deceleration for particles of different sizes. The exponential deceleration of iron particles was predicted because iron was in a molten state for longer than alumina, as observed from the temperature-time curve of the thermite reaction. With increasing viscosity (Figure 2), particle motion would naturally be affected. For instance, in Figure 5, as the particle size increases, the velocity gradient slope is greater and the particles decelerate faster. However, this does not drastically happen for alumina, whereby the particle speed gradient curve tends to become zero almost at the same time regardless of particle size. Nevertheless, the gradient of velocity in the radial direction for iron significantly correlates to particle size.

When the velocity gradient becomes zero at this stage, there might not be molten phase diffusion; but the solid-state diffusion phenomenon is probably still mainly happening[29,30] for iron particles. Solid-s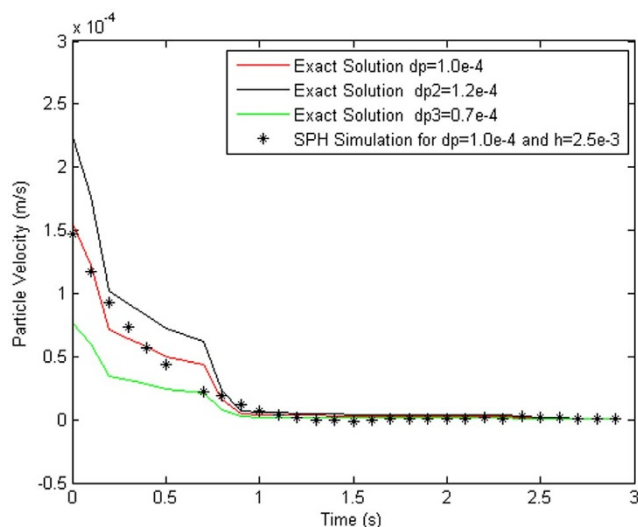tate diffusion is widely accepted with respect to combustion synthesis processing. When the material has less motion in the liquid phase and owing to the in-situ high temperature gradient, the particles diffuse into each other and form intermetallics, alloys or cermets. If this phenomenon combines with centrifugal force, there would be extra external force acting beyond the viscosity increment, which poses resistance to the particles' motion. Finally, there would be a greater amount of the obtained product than expected. Velocity and velocity gradient results are in agreement with the experimental evidence of the centrifugal thermite and molten iron infiltration in the TiC pellet discussed earlier[8]. Moreover, the simulation results help infer the reason why alumina particles are observed at the TiC pellet boundary and why iron particles infiltrated the TiC porous medium (Figure 1).

The indirect correlation with viscosity change over time is manifest in Figure 6. The particle position becomes zero exactly when the velocity gradient becomes zero. The particle motion completely stops after the solidification process takes place for 3 seconds. Sudden changes in molten particle position are obvious when the viscosity decreases, and the particles have no relative motion and displacement after 0.7 s from the SHS reaction. However, the particles may experience solid diffusion. Consequently, the particle diffusion speed tends toward zero as time increases.

Again, it is understood that alumina particles are not moving toward the TiC pellet as the iron particles are (Figure 6). The alumina particles are mostly deposited at the internal boundary of the TiC pellet (Figure 1), so-called the top surface, due to the rapid increase in relative viscosity (Figure 2). Meanwhile, the viscosity of alumina increases in a fraction of a second, whereas the iron viscosity does not increase to the same extent. Therefore, iron will continue to penetrate or diffuse into the TiC porous media and alumina flow stops. The results in Figure 6 indicate that the alumina particles are expected to diffuse into TiC at a depth between 15 to 45 μm, depending on particle size. The FESEM micrograph in Figure 1 (a) and its corresponding EDS elemental analysis (Table 1) strongly support the simulation MSPH results. It is thus clear why alumina accumulated at the innermost layer relative to the rotation axis, but the solid alumina layer isolated the iron particles. However, the iron particles remained in liquid phase and were able to stay in the molten medium for a longer period than alumina (Figure 8). This phenomenon allows the iron particles to wet and infiltrate the TiC porous media, and form a stronger composite structure. Figure 8 (b) displays how the iron particles surround TiC in zone (III). Therefore, the above-mentioned simulation has excellent potential in controlling particle diffusion.
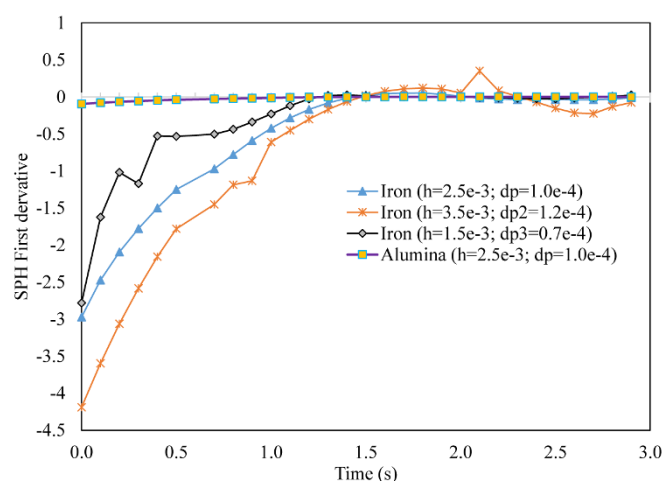

Figure 4 | Alumina particle radial velocity (for three particle sizes) and the corresponding MSPH simulation.

Figure 5 | MSPH estimates of the particle velocity gradient (PVG) in the radial direction for three different alumina and iron particle sizes.
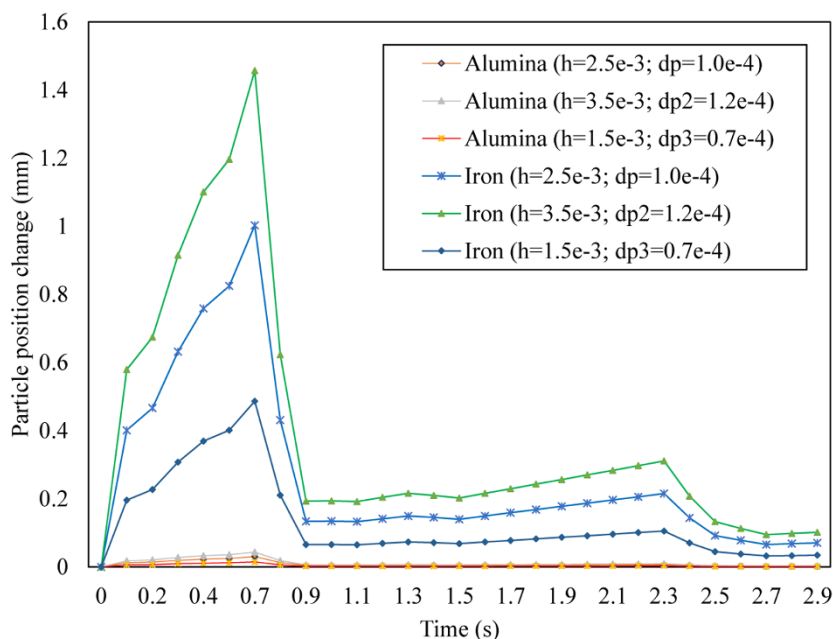
Figure 6 | Instantaneous change in radial direction versus time of alumina and iron particles during deposition.

As explained earlier, the total mass and volume of the solution domain were approximated based in the particle method. As the number of particles approaches infinity, the approximation error moves toward zero. Essentially, both real and approximated solution domains are identical, thus, the exact analytical and MSPH solutions must be the same. However, because the simulation process included a limited number of particles, simulation error was present. Therefore, for a small number of particles the approximation error is big given that the particles are large. In the case of size dp2, shown in Figure 3 and Figure 5, the particle size was 120 µm, which is the largest among the simulated cases. Thus, it is anticipated that the simulation error would be the largest. This helps clarify the significant difference in the two models' results. Moreover, the viscosity equation was also approximated based on particle size. Similarly, for particle size dp2, the viscosity approximation error was the largest. Especially at 0.9 and 2.1 seconds from the beginning of the reaction, the approximation error was quite significant (Figure 3). Given that at these two points abrupt changes in viscosity value occurred, particle approximation is presumed to be even poorer.

The MSPH simulation results are in agreement with the experimental observations. Alumina viscosity increases faster than iron, and alumina protects iron from external heat exchange, the iron remains in the molten medium longer than alumina. This phenomenon allows the iron particles to wet and infiltrate the TiC porous media and form a strong composite. Mathematical modeling of particle deposition velocity and viscosity can describe the process of Fe infiltration versus time. Melt viscosity increment due to the decrease in temperature leads to a significant speed reduction of particle deposition onto TiC. The MSPH method provides a very good estimation of velocity and velocity gradient of iron and alumina molten particles. The MSPH estimates the magnitude of molten iron and alumina infiltration, the depth, velocity and velocity gradient. The velocity gradient of particles reveals that the product velocity decelerates as the viscosity increases versus time. The prediction is in agreement with the experimental results, microstructure, and EDS observations.

Methods

Experimental methods. A centrifugal thermite (CT) machine facilitated rapid centrifugal acceleration as well as the temperature increase during the experiment. A

bilayer graphite-steel compacted mold was fixed inside the CT reaction chamber. A high performance infrared thermometer, Raytek MM1MHSF3L, recorded the experimental real-time temperature data. The detailed procedure of using the centrifugal machine for thermite processing in metallic pipes is explained in recently published literature[31].

The starting materials, namely Al (<75 µm, 99% purity, Sigma Aldrich) and Fe_2O_3 (<5 µm, 97% purity, Sigma Aldrich) powders were dried for 8 hours and mixed in a Retsch PM 200 Planetary Ball Mill for 4 hours at 30-minute intervals. The green powder stoichiometric mixture was prepared according to the following reaction equation (1)[32].

$$Fe_2O_3 + 2Al \rightarrow Al_2O_3 + 2Fe, \ \Delta H = -836 \ kJmol^{-1} \tag{1}$$
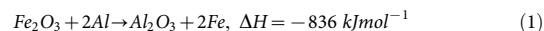
Titanium (Sigma Aldrich, -100 mesh, 99.7% purity) and carbon (Sigma Aldrich, -1000 mesh, 99.9% purity) elemental powders were dried for 7 hours at 125°C, following which they were mixed using a Planetary Ball Mill (Retsch PM 200) according to the reaction equation (2):

$$Ti + C \rightarrow TiC, \ \Delta H = -183 \ kJmol^{-1} \tag{2}$$
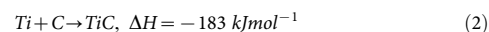
A 75 mm long carbon steel pipe with inner and outer diameters of 69 mm and 75 mm, respectively, served as a bulk holder for graphite. The dried Ti + C green powder was compressed into a pellet. The pellet was then inserted into the graphite mold's pre-defined location as shown in Figure 7. The pellet was positioned near the head of the tube because of the higher thermal gradient[33].

The thermite mixture was fed into the tube. The rotation speed was subsequently increased to 280 g acceleration, followed by igniting an electric arc with a graphite electrode at the entrance of the tube. The onset of the thermite reaction was trailed by the titanium and carbon reaction, which occurred in response to the heat generated by the thermite (first) reaction. The released temperature was recorded by an infrared pyrometer. The detailed process and characterizations are explained extensively in a recently published paper by the authors[8].

Modeling and simulation of SHS using modified smoothed particle hydrodynamics (MSPH). *Implementation of MSPH in the centrifugal thermite method.* Figure 8 shows a schematic that represents the centrifugal SHS components in particle approximation. The TiC porous pellet, Al_2O_3 and Fe Molten particles are shown just after the SHS reaction started (Figure 8 (a)). The representation of the infiltration of molten alumina and iron particles into the TiC pellet are seen in Figure 8 (b) and (c), which show the TiC pellet just after particle infiltration stopped and the particles approached the inner surface of the steel pipe. In this model, all particles are distinct in volume.

Comprehensive MSPH formulations are provided in literature[26,34]. The MSPH method was adapted to the TiC-Fe-Al_2O_3 centrifugal SHS process. Cylindrical coordinates (r,θ,z) were used to analyze the axisymmetric motion of particles, since the reaction occurred inside a cylindrical steel pipe. The function, *f*, describing a displacement variable, is independent of the angular position, θ, of a particle point. Particle approximation using MSPH is mainly dependent on the Taylor series expansion of function f(r,z) about point (r$_i$,z$_i$), which is given as:
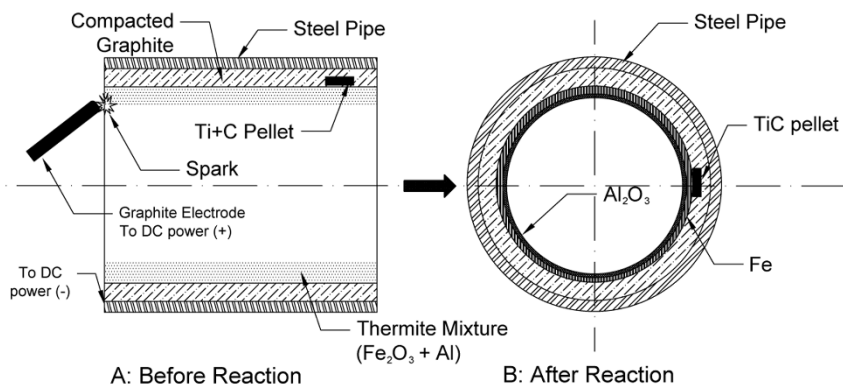
Figure 7 | Schematic setup of the centrifugal thermite-assisted Ti-based functionally graded coating process; (A) before reaction, (B) after reaction.

$$f(r,z) = f(r_i,z_i) + \frac{\partial f}{\partial r}(r-r_i) + \frac{\partial f}{\partial z}(z-z_i) + \frac{1}{2}\frac{\partial^2 f}{\partial r^2}(r-r_i)^2$$
$$+ \frac{1}{2}\frac{\partial^2 f}{\partial z^2}(z-z_i)^2 + \frac{\partial^2 f}{\partial r \partial z}(r-r_i)(z-z_i) + \ldots \quad (3)$$

where the derivatives are assessed at point $x = (r_i,z_i) = (x_i, y_i)$. Neglecting the third and higher order derivative terms on the right side of equation (3) and multiplying both sides of the equation with a positive-value kernel function $W(x - \zeta, h)$ of compact support, or a smoothing length of $2h$, determines the number of particles involved in the approximation. The center of the particle position, x, its first and second derivatives, then integrate the resulting equations over the solution domain. The integration domain can be replaced by the compact support of the kernel function since the kernel function is zero when the support is above $2h$. In this way, it is possible to estimate and write particle position, particle velocity, and particle velocity gradient in matrix form:

$$BF = L \text{ or } B_{IJ}F_J = L_I \quad I = 1,2,3,\ldots 6 \quad (4)$$

Where

$$F = \begin{Bmatrix} f_i \\ f_{xi} \\ f_{yi} \\ f_{xxi} \\ f_{yyi} \\ f_{xyi} \end{Bmatrix}; \quad L = \begin{Bmatrix} \sum_{j=1}^{N} f_i W_{ij} m_j/\rho_j \\ \sum_{j=1}^{N} f_i W_{ij,x} m_j/\rho_j \\ \sum_{j=1}^{N} f_i W_{ij,y} m_j/\rho_j \\ \sum_{j=1}^{N} f_i W_{ij,xx} m_j/\rho_j \\ \sum_{j=1}^{N} f_i W_{ij,yy} m_j/\rho_j \\ \sum_{j=1}^{N} f_i W_{ij,xy} m_j/\rho_j \end{Bmatrix};$$

$$B = \begin{bmatrix} \sum_{j=1}^{N} \varphi_1 W_{ij} m_j/\rho_j & \sum_{j=1}^{N} \varphi_2 W_{ij} m_j/\rho_j & & \sum_{j=1}^{N} \varphi_6 W_{ij} m_j/\rho_j \\ \sum_{j=1}^{N} \varphi_1 W_{ij,x} m_j/\rho_j & \sum_{j=1}^{N} \varphi_2 W_{ij,x} m_j/\rho_j & & \sum_{j=1}^{N} \varphi_6 W_{ij,x} m_j/\rho_j \\ \sum_{j=1}^{N} \varphi_1 W_{ij,y} m_j/\rho_j & \sum_{j=1}^{N} \varphi_2 W_{ij,y} m_j/\rho_j & & \sum_{j=1}^{N} \varphi_6 W_{ij,y} m_j/\rho_j \\ \sum_{j=1}^{N} \varphi_1 W_{ij,xx} m_j/\rho_j & \sum_{j=1}^{N} \varphi_2 W_{ij,xx} m_j/\rho_j & \ldots \ldots \ldots \ldots & \sum_{j=1}^{N} \varphi_6 W_{ij,xx} m_j/\rho_j \\ \sum_{j=1}^{N} \varphi_1 W_{ij,yy} m_j/\rho_j & \sum_{j=1}^{N} \varphi_2 W_{ij,yy} m_j/\rho_j & & \sum_{j=1}^{N} \varphi_6 W_{ij,yy} m_j/\rho_j \\ \sum_{j=1}^{N} \varphi_1 W_{ij,xy} m_j/\rho_j & \sum_{j=1}^{N} \varphi_2 W_{ij,xy} m_j/\rho_j & & \sum_{j=1}^{N} \varphi_6 W_{ij,xy} m_j/\rho_j \end{bmatrix};$$

and

$$\varphi_1 = 1, \quad \varphi_2 = x_j - x_i, \quad \varphi_3 = y_j - y_i,$$
$$\varphi_4 = \frac{1}{2}(x_j - x_i)^2, \quad \varphi_5 = \frac{1}{2}(y_j - y_i)^2, \quad \varphi_6 = (x_j - x_i)(y_j - y_i)$$

To obtain the solution for F, matrix B should be non-singular. This condition is already satisfied since the functions φ_i are linearly independent and the number of particles in the compact support of the kernel function W for particles is at least 6. All derivatives of kernel function W appearing in matrix B, must not be constants. Therefore, to easily approximate and calculate the radial positions and infiltration rates of iron and alumina into TiC in the centrifugal-assisted SHS method, the revised Gauss function $W(x-\xi, h)$ in equations (4) is used as the kernel function.
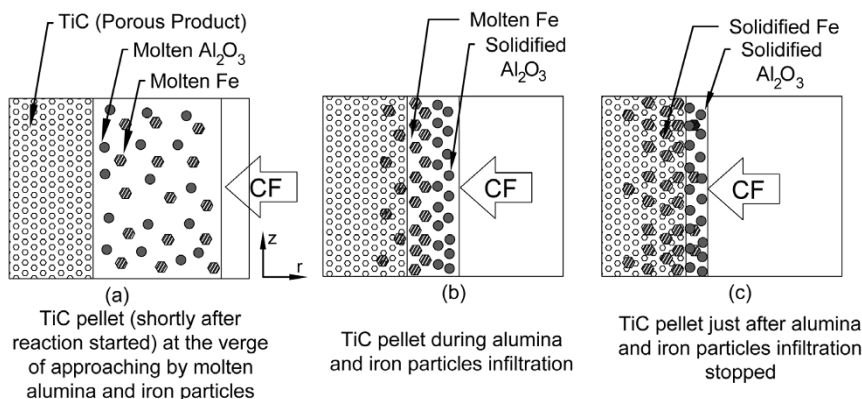

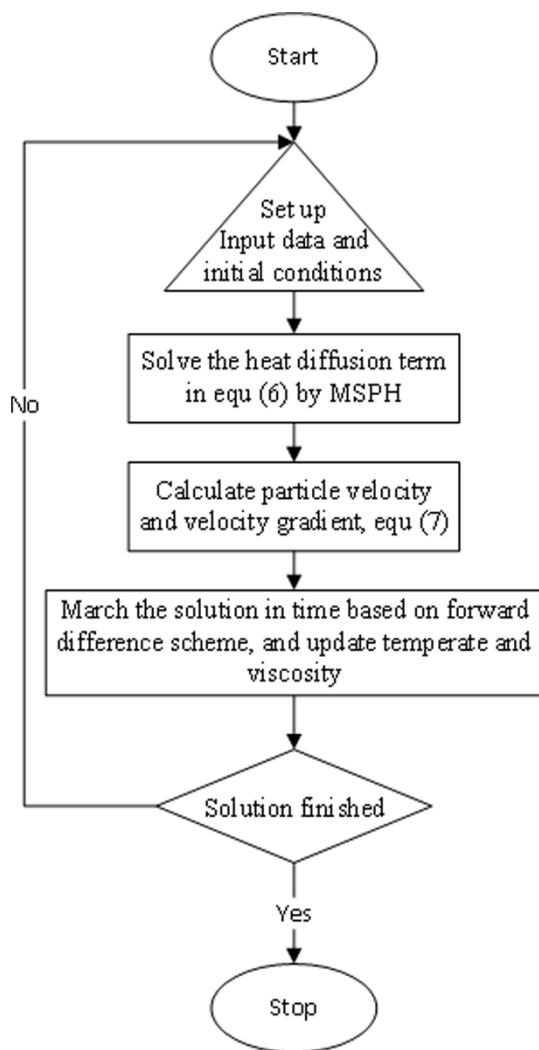**Figure 8 | Schematic of a TiC pellet and the molten alumina and iron particles at different positions.**

$$\rho C_p \frac{\partial T}{\partial t} = q - k\left(\frac{\partial^2 T}{\partial r^2} + \frac{1}{r}\frac{\partial T}{\partial r} + \frac{\partial^2 T}{\partial z^2}\right) \qquad (6)$$

where T is the transient temperature, t the time during the process, k is thermal conductivity, ρ is density, C_p is the heat capacity, and q is the rate of heat generated during the reaction process. The last term in equation (6) functions as a heat sink from the reaction zone in the SHS process. The heat is consumed in preheating the reacted mixture. With the help of the initial conditions, the MSPH method can be utilized to solve equation (6). The starting mixture temperature and activation energy are given. Equation (6) is written for particle i and the values of T_{rri}, T_{ri} and T_{zzi}, which are similar to T_{xxi}, T_{xi} and T_{yyi}, and are determined by solving the linear simulation equations (4).

$$f_{xi} = T_{xi} = \frac{\partial T(r_i,z_i)}{\partial r} = \frac{\partial T(x_i,y_i)}{\partial x} = B_{I2}L_1 = \sum_{j=1}^{N} B_{I2}\,W_{ij,x}\,m_j/\rho_j.T_j$$

$$f_{xxi} = T_{xxi} = \frac{\partial^2 T(r_i,z_i)}{\partial r^2} = \frac{\partial^2 T(x_i,y_i)}{\partial x^2} = B_{I4}L_1 = \sum_{j=1}^{N} B_{I4}\,W_{ij,xx}\,m_j/\rho_j.T_j$$

$$f_{yyi} = T_{yyi} = \frac{\partial^2 T(r_i,z_i)}{\partial z^2} = \frac{\partial^2 T(x_i,y_i)}{\partial y^2} = B_{I5}L_1 = \sum_{j=1}^{N} B_{I5}\,W_{ij,yy}\,m_j/\rho_j.T_j$$

The solution is marching forward in time by the conditionally stable forward-difference scheme. Upon obtaining the temperature distribution, it is possible to calculate the viscosity, particle velocity and velocity gradient.

Solving the particle velocity and velocity gradient equations. Form Stoke's formula for particle motion in fluid, as well as normal gravity and equilibrium of forces on a particle in the SHS process under centrifugal acceleration[8], the radial particle velocity $V(T, t)$ as a function of temperature and time is given as:

$$V(T_c,t) = \frac{d^2(\rho_o - \rho_m)(39.4Rn^2 + g)}{18\eta} \qquad (7)$$

$$\eta(T_c) = \eta_o\, exp\left(\frac{Q}{R_g.T_c}\right) \qquad (8)$$

where R is the current radial position of the particles, $\eta(T_c)$ is the current viscosity of the molten metal, Q is total activation energy, and the gas constant is R_g. The rotation speed per second is n, g is the acceleration of gravity, and T_c is the temperature. Particle size is d whereas ρ_o and ρ_m are the particle density and melt density, respectively.

Since the determinant of matrix B is nonzero, its inverse, B^{-1}, exists. Thus, equation (4) can be rewritten as:

$$F = B^{-1}T \ or \ F_J = B_{IJ}^{-1}T_I, \quad I = 1,2,3,\dots 6 \qquad (9)$$

Equation (8) gives the values of function f (velocity, V) and its first-order and second-order derivatives at point $\mathbf{x} = (x_i, y_i)$ in terms of velocity values at points neighboring $\mathbf{x}$. Based on equation (9), MSPH approximation of radial velocity and radial velocity gradient can be explicitly written as:

$$f_i = V(r_i,z_i) = V(x_i,y_i) = B_{I1}T_1 = \sum_{j=1}^{N} B_{I1}\,W_{ij}\,m_j/\rho_j.V_j \qquad (10)$$

$$f_{xi} = \frac{\partial V(r_i,z_i)}{\partial r} = \frac{\partial V(x_i,y_i)}{\partial x} = B_{I2}T_1 = \sum_{j=1}^{N} B_{I2}\,W_{ij,x}\,m_j/\rho_j.V_j \qquad (11)$$

It is evident that for the MSPH method, kernel approximation of the velocity gradient is given in terms of the integration of the first-order derivative of W(x-ξ, h) over its compact support.

Coding and simulation procedure. MATLAB, Mathworks ® version 2012a, was employed to write the MSPH for solving equations (6) and (7). A flowchart of the solution procedure is shown in Figure 9. First, using the initial condition, the heat condition equation is solved and once the temperature distribution is known, viscosity, particle radial velocity, and radial velocity gradient are calculated. The solution marches forward in time by the conditionally stable forward-difference scheme. The time increment employed is 1 μs. Interaction radius or smoothing length (h) is chosen such that 15–20 particles are interacting on average[26], where the total number of particles is 29. The MSPH simulation parameters are listed in Table 1.

MSPH simulation of iron and alumina particles was conducted with parameters extracted from existing literature. Molten iron $\eta_o = 0.0065$ kg/m.s[35], total activation energy, $Q = 706$ kJ/mol of Al-Fe_2O_3 and Ti-$C^{36,37}$, gas constant $R_g = 8.31441$ J/K.mol[38], and $\eta_o = 0.052$ N.s/m² is the liquid viscosity of alumina at 2408 K[39]. The other thermophysical properties are listed in Table 3.

Figure 9 | MSPH computing method to predict particle properties.

$$W(x-\xi,h) = \begin{cases} \dfrac{1.10081}{(h\sqrt{\pi})^2}\left(e^{-|x-\xi|^2/h^2} - e^{-4}\right); & |x-\xi| \le 2h, \\ 0 & ; \quad |x-\xi| > 2h. \end{cases} \qquad (5)$$

In the present SHS model, smoothing length, or interaction radius (h), is selected such that on average 15–20 particles are interacting[26].

Solving the heat balance equation. Based on the geometric configuration of the SHS process, the temperature distribution is symmetric about the z-axis. Therefore, the thermal condition problem is simply a two-dimensional axisymmetric problem. For a unity volume, the heat balance equation or the transient heat flow governing equation is:

Table 3 | Thermophysical properties of Fe-Al_2O_3-TiC particles

	Reaction 1 [equation (1)]		Reaction 2 [equation (2)]
	Fe	Al_2O_3	TiC
C, J kg⁻¹ K⁻¹	473	880	881.98
m, kg	9.19E-02	8.39E-02	3.30E-03
ρ_o, kg m⁻³	7800[40]	3950[41]	4930[42]
ρ_m, kg m⁻³	2700[43]	2750[44]	-
K, w/m.K	47		
Cp, kJ/kg.K	0.49		
Q, kJ mol⁻¹		145	560
q, kJ mol⁻¹		836	183[45]

1. Song, M. S., Ran, M. W. & Kong, Y. Y. In situ fabrication of ZrC ceramic obtained by self-propagating high-temperature synthesis from Al-Zr-C elemental powders. *Int. J. Refract. Met. Hard Mater* **29**, doi: 10.1016/j.ijrmhm.2011.01.013 (2011).

2. Munir, Z. A. in *Encyclopedia of Materials: Science and Technology* [(eds K. H. Jürgen, Buschow *et al.*)] 8323–8327 (Elsevier, 2001).

3. Odawara, O. Mass-Forced SHS Technology of Ceramic Materials. *Adv. Sci. Technol.* **63**, 302–311, doi: 10.4028/www.scientific.net/AST.63.302 (2010).

4. Zhu, Y., Sun, S., Ni, H. & Huang, M. Study on microstructure and properties of ceramic-lined composite steel pipes produced by centrifugal-SHS process. *Key Eng. Mater.* **464**, 434–437, doi: 10.4028/www.scientific.net/KEM.464.434 (2011).

5. Merzhanov, A. G. Thermally coupled SHS reactions. *Int. J. Self Propag. High Temp. Synth.* **20**, 61–63, doi: 10.3103/s1061386211010109 (2011).

6. Gao, F., Guo, Z. & Lin, T. Preparation of W-C-Fe cermet lined steel pipes by SHS-centrifugal process. *J. Univ. Sci. Technol. Beijing* **30**, 648–651 (2008).

7. Wang, Y.-F. & Yang, Z.-G. Finite element analysis of residual thermal stress in ceramic-lined composite pipe prepared by centrifugal-SHS. *Mater. Sci. Eng., A* **460–461**, 130–134, doi: 10.1016/j.msea.2007.01.017 (2007).

8. Mahmoodian, R., Hassan, M. A., Rahbari, R. G., Yahya, R. & Hamdi, M. A novel fabrication method for TiC-Al₂O₃-Fe functional material under centrifugal acceleration. *Composites, Part B* **50**, 187–192, doi: 10.1016/j.compositesb.2013.02.016 (2013).

9. Yang, Y.-F., Wang, H.-Y., Liang, Y.-H., Zhao, R.-Y. & Jiang, Q.-C. Effect of C particle size on the porous formation of TiC particulate locally reinforced steel matrix composites via the SHS reaction of Ni–Ti–C system during casting. *Effect of C particle size on the porous formation of TiC particulate locally reinforced steel matrix composites via the SHS reaction of Ni–Ti–C system during casting* **474**, 355–362, doi: 10.1016/j.msea.2007.04.061 (2008).

10. Birman, V. & Byrd, L. W. Modeling and Analysis of Functionally Graded Materials and Structures. *Appl. Mech. Rev.* **60**, 195–216, doi: 10.1115/1.2777164 (2007).

11. Gennari, S., Maglia, F., Anselmi-Tamburini, U. & Spinolo, G. SHS (Self-sustained high-temperature synthesis) of intermetallic compounds: effect of process parameters by computer simulation. *Intermetallics* **11**, 1355–1359, doi: 10.1016/S0966-9795(03)00179-1 (2003).

12. Zhang, G., Xiao, G. & Fan, Q. Numerical modeling of field-activated combustion synthesis process of the B4C system. *Mater. Res. Bull.* **46**, 345–349, doi: 10.1016/j.materresbull.2010.12.019 (2011).

13. Gao, J. W. & Wang, C. Y. Modeling the solidification of functionally graded materials by centrifugal casting. *Mater. Sci. Eng., A* **292**, 207–215, doi: 10.1016/s0921-5093(00)01014-5 (2000).

14. Advani, A. H. *et al.* Dynamic modelling of material and process parameter effects on self-propagating high-temperature synthesis of titanium carbide ceramics. *J. Mater. Sci.* **27**, 3309–3317, doi: 10.1007/BF01116030 (1992).

15. Song, I., Wang, L., Wixom, M. & Thompson, L. T. Self-propagating high temperature synthesis and dynamic compaction of titanium diboride/titanium carbide composites. *J. Mater. Sci.* **35**, 2611–2617, doi: 10.1023/A,1004731532616 (2000).

16. Gingold, R. A. & Monaghan, J. J. Smoothed particle hydrodynamics-theory and application to non-spherical stars. *Mon. Not. R. Astron. Soc.* **181**, 375–389 (1977).

17. Lucy, L. B. A numerical approach to the testing of the fission hypothesis. *Astron. J.* **82**, 1013–1024 (1977).

18. Monaghan, J. J. A turbulence model for Smoothed Particle Hydrodynamics. *Eur. J. Mech. B-Fluid* **30**, 360–370, doi: 10.1016/j.euromechflu.2011.04.002 (2011).

19. Monaghan, J. J. Smoothed particle hydrodynamics. *Rep. Prog. Phys.* **68**, 1703, doi: 10.1088/0034-4885/68/8/R01 (2005).

20. Liu, M. & Liu, G. Smoothed particle hydrodynamics (SPH): an overview and recent developments. *Arch. Comput. Method E.* **17**, 25–76, doi: 10.1007/s11831-010-9040-7 (2010).

21. Cleary, P. W. & Monaghan, J. J. Conduction Modelling Using Smoothed Particle Hydrodynamics. *J. Comput. Phys.* **148**, 227–264, doi: 10.1006/jcph.1998.6118 (1999).

22. Muhammad, N., Rogers, B. D. & Li, L. Understanding the behaviour of pulsed laser dry and wet micromachining processes by multi-phase smoothed particle hydrodynamics (SPH) modelling. *J. Phys. D: Appl. Phys.* **46**, 095101, doi: 10.1088/0022-3727/46/9/095101 (2013).

23. Price, D. J. Smoothed particle hydrodynamics and magnetohydrodynamics. *J. Comput. Phys.* **231**, 759–794, doi: 10.1016/j.jcp.2010.12.011 (2012).

24. Takaffoli, M. & Papini, M. Material deformation and removal due to single particle impacts on ductile materials using smoothed particle hydrodynamics. *Wear* **274–275**, 50–59, doi: 10.1016/j.wear.2011.08.012 (2012).

25. Cleary, P. *et al.* Modeling cast systems using smoothed-particle hydrodynamics. *JOM* **56**, 67–70, doi: 10.1007/s11837-004-0038-1 (2004).

26. Zhang & Batra, R. C. Modified smoothed particle hydrodynamics method and its application to transient problems. *Comput. Mech.* **34**, 137–146, doi: 10.1007/s00466-004-0561-5 (2004).

27. Belytschko, T., Rabczuk, T., Huerta, A. & Fernández-Méndez, S. in *Encyclopedia of Computational Mechanics* (John Wiley & Sons, Ltd, 2004).

28. Meng, Q. S. *et al.* Microstructure and mechanical properties of multilayer-lined composite pipes prepared by SHS centrifugal-thermite process. *Mater. Sci. Eng., A* **456**, 332–336, doi: 10.1016/j.msea.2006.12.016 (2007).

29. Feng, K. Q., Hong, M., Xiong, J., Fan, H. Y. & Guo, Z. X. Mechanism of combustion synthesis of TiC-Fe composites under the action of an electric field. *Powder Metall.* **55**, 235–241, doi: 10.1179/1743290111Y.0000000005 (2012).

30. Fan, Q., Chai, H. & Jin, Z. Mechanism of combustion synthesis of TiC–Fe cermet. *J. Mater. Sci.* **34**, 115–122, doi: 10.1023/A,1004430028260 (1999).

31. Mahmoodian, R., Rahbari, R. G., Hamdi, M. & Sparham, M. A new attempt to adopt a machine for SHS lining ceramics inside pipes. *High Temp. Mater. Processes* **16**, 15–23, doi: 10.1615/HighTempMatProc.2012004708 (2012).

32. Odawara, O. in *International Symposium on Combustion and Plasma Synthesis of High Temperature Materials.* [(ed Holt, J. B. & Munir, Z. A.)] [179–185] (VCH Publishers, Inc., 1990).

33. Mahmoodian, R., Rahbari, R. G., Hamdi, M., Hassan, M. A. & Sparham, M. The Effects of an Unexpected Ceramic Coating Phase at the Head of a Pipe on Joining and Postprocessing of a Ceramic-Lined Composite Pipe. *JOM* **65**, 80–85, doi: 10.1007/s11837-012-0498-7 (2013).

34. Batra, R. C. & Zhang, G. M. Modified Smoothed Particle Hydrodynamics (MSPH) basis functions for meshless methods, and their application to axisymmetric Taylor impact test. *J. Comput. Phys.* **227**, 1962–1981, doi: 10.1016/j.jcp.2007.10.001 (2008).

35. Ho, Y.-H. & Hwang, W.-S. The Analysis of Molten Steel Flow in Billet Continuous Casting Mold. *ISIJ Int.* **36**, 1030–1035, doi: 10.2355/isijinternational.36.1030 (1996).

36. Fan, R. H., Lü, H. L., Sun, K. N., Wang, W. X. & Yi, X. B. Kinetics of thermite reaction in Al-Fe₂O₃ system. *Thermochim. Acta* **440**, 129–131, doi: 10.1016/j.tca.2005.10.020 (2006).

37. Munoz, J. D., Arizmendi, A., Mendoza-Allende, A. & Montemayor-Aldrete, J. A. High temperature activation energy for plastic deformation of titanium carbide single crystals as a function of the C: Ti atom ratio. *J. Mater. Sci.* **32**, 3189–3193, doi: 10.1023/a,1018654818631 (1997).

38. Balout, B. & Litwin, J. Mathematical Modeling of Particle Segregation During Centrifugal Casting of Metal Matrix Composites. *J. Mater. Eng. Perform.* **21**, 450–462, doi: 10.1007/s11665-011-9873-8 (2012).

39. Quang, V. V. *Dynamical, Rheological and Thermal Studies of High Temperature Oxide Liquids* PhD thesis, Aberystwyth University, (2008).

40. Vardelle, A., Themelis, N. J., Dussoubs, B., Vardelle, M. & Fauchais, P. Transport and chemical rate phenomena in plasma sprays. *High Temp. Mater. Processes* **1**, 295–313 (1997).

41. Rahimian, M., Parvin, N. & Ehsani, N. Investigation of particle size and amount of alumina on microstructure and mechanical properties of Al matrix composite made by powder metallurgy. *Mater. Sci. Eng., A* **527**, 1031–1038, doi: 10.1016/j.msea.2009.09.034 (2010).

42. Chan, Y. & Choi, S. Numerical simulations of inductive-heated float-zone growth. *J. Appl. Phys.* **72**, 3741–3749, doi: 10.1063/1.352294 (1992).

43. Mihok, Ľ., Demeter, P., Baricova, D. & Seilerova, K. Utilization of ironmaking and steelmaking slags. *Metalurgija* **45**, 163–168 (2006).

44. Glorieux, B., Millot, F., Rifflet, J. C. & Coutures, J. P. Density of Superheated and Undercooled Liquid Alumina by a Contactless Method. *Int. J. Thermophys.* **20**, 1085–1094, doi: 10.1023/A,1022650703233 (1999).

45. Mahmoodian, R., Hassan, M. A., Hamdi, M., Yahya, R. & Rahbari, R. G. In-situ TiC-Fe-Al₂O₃-TiAl/Ti₃Al composite coating processing using centrifugal assisted combustion synthesis. *Composites Part B: Engineering* **In press**, doi: 10.1016/j.compositesb.2013.12.016 (2014).

Acknowledgments

Author contributions

R.M. conducted the research experiment and contributed to the discussions, theoretical analysis and writing of the manuscript along with M.A.N.A. and M.H. All authors reviewed the manuscript. Mr. Ali Mahmoodian has facilitated the design and fabrication of the centrifugal SHS reaction chamber at Azarin Kar IND. Co.

Additional information